Statistical analysis of magnetic domain wall dynamics to quantify Dzyaloshinskii-Moriya interaction

Xinwei Shi, Panpan Fang, Chen Sun, and Fuxiang Li *
School of Physics and Electronics, Hunan University, Changsha 410082, China

(Received 11 June 2023; revised 23 September 2023; accepted 24 October 2023; published 9 November 2023)

We utilize statistical tools to analyze the magnetic domain wall dynamics in a nanostrip, which can quantify the magnitude and reveal the effects of interfacial Dzyaloshinskii-Moriya interaction (DMI). We find that two peaks in the velocity frequency spectrum exist, the magnitude ratio of which can be used to determine the DMI strength. Our approach is validated by the collective-coordinate model and is demonstrated to be robust against thermal noise and material impurities. Moreover, the third-order cumulant and third-order time-dependent correlation function of velocity are calculated and yield valuable information regarding the asymmetry induced by DMI. Our findings offer efficient analysis tools to understand the physical process of domain wall dynamics under DMI and exotic magnetic phenomena.

DOI: 10.1103/PhysRevB.108.174416

I. INTRODUCTION

Dzyaloshinskii-Moriya interaction (DMI) plays a fundamental role in the stabilization of exotic spin structures, such as spin spirals [1,2], chiral domain walls [3,4], and magnetic skyrmions [5–7]. These spin structures can be driven by electric current or external magnetic field with a high level of efficiency and thus are particularly attractive as promising information carriers for future spintronics technologies [5,8]. Therefore, accurately and reliably quantifying the DMI in magnetic materials is of utmost importance for identifying potential materials for spintronic-based devices.

One particularly interesting and commonly studied magnetic system is a thin magnetic film with perpendicular magnetic anisotropy due to the fast domain wall motion driven by the electric current or magnetic field [9–12]. In these multilayers consisting of an ultrathin ferromagnetic film in contact with a heavy metal, interfacial DMI can be induced at the interface due to the broken inversion symmetry and the large spin-orbit coupling of the heavy metal atoms [13,14]. It has been demonstrated that DMI strongly affects the domain wall internal spin texture, domain wall dynamics, and spin wave propagation [15,16]. In return, by exploiting the unique properties and peculiar phenomena induced by DMI, such as the Walker breakdown in field-driven domain wall motion and nonreciprocity in spin wave propagation, different experimental techniques have been developed to quantify DMI strength in combination with a simple analytical theoretical model [17]. For example, using Brillouin light spectroscopy, the DMI strength can be obtained by monitoring nonreciprocal propagation in the Damon-Eshbach geometry [18,19]. In the creep regime of domain wall motion, the asymmetric expansion of a magnetic bubble under in-plane magnetic field and in the presence of DMI can also be utilized as a measure of DMI strength [17,20]. Even though different experimental techniques have been developed to quantify the DMI, each technique has its own advantages and disadvantages and often produces contradictory values even for the same system. Moreover, most of the experimental techniques also require either high-precision imaging of the domain wall structure or a high-quality magnetic material [17].

Here, we introduce statistical tools to analyze the domain wall dynamics in a magnetic nanostrip in the presence of DMI. We show that, rather than simple averaging of instantaneous velocity [21,22], statistical analysis reveals more detailed information concealed in the noisy data of magnetic domain wall dynamics. By fast Fourier transformation of time-varying domain wall velocity, we observe the emergence of two peaks in the velocity frequency spectrum in the presence of interfacial DMI. By combining the micromagnetic simulation and analytical analysis based on the collective-coordinate model, we show that, in the precessional regime, the magnitude ratio of the low-frequency mode to the high-frequency mode in the velocity frequency spectrum is linearly proportional to the DMI strength but is independent of external magnetic field. This ratio can thus be utilized to experimentally quantify the DMI strength in ferromagnetic films. Further, this method for the velocity frequency spectrum is demonstrated to be robust even in the presence of external noise and magnetic pinning disorder, which is crucial for accurately measuring the strength of DMI in real materials. Moreover, the third-order cumulant and third-order time-dependent correlation function of velocity are calculated and shown to yield valuable information regarding the asymmetry induced by DMI. The proposed statistical analysis provides a robust method for quantifying micromagnetic parameters and uncovers more detailed information about DMI.

The remainder of this paper is structured as follows. In Sec. II, we present the theoretical model for domain wall (DW) motion in ferromagnetic films with interfacial Dzyaloshinskii-Moriya interaction and introduce the velocity frequency spectrum that can be used to quantify DMI strength. Subsequently, in Sec. III, we introduce the

*fuxiangli@hnu.edu.cn

collective-coordinate model to verify the simulation results and explain the underling physics of the velocity frequency spectrum. In Sec. IV, we demonstrate the robustness of the velocity frequency spectrum by considering the domain wall dynamics in the presence of external noise and pinning disorder. Moreover, in Sec. V, we show that considering the third-order cumulant and third-order time-correlation function can reveal the intrinsic asymmetry induced by DMI. To complete our study, in Sec. VI, we provide the results of domain wall dynamics driven by electric current. Finally, we conclude with a brief discussion and summary of the key results in Sec. VII.

II. MODEL AND METHOD

A. Model and setup

We start by considering the field-driven domain wall dynamics of a thin magnetic film with perpendicular magnetic anisotropy. The film is patterned into a long strip which provides an ideal setup to study domain wall propagation. We use the GPU accelerated micromagnetic simulation program MUMAX3 to simulate the DW dynamics [23]. This program solves the space- and time-dependent reduced magnetization $\boldsymbol{m}(\mathbf{r}, t)$ in the Landau-Lifshitz-Gilbert (LLG) equation,

$$\frac{\partial \boldsymbol{m}}{\partial t} = -\gamma \boldsymbol{m} \times \boldsymbol{H}_{\text{eff}} + \alpha \boldsymbol{m} \times \frac{\partial \boldsymbol{m}}{\partial t}. \tag{1}$$

Here, γ is the gyromagnetic ratio, α is the dimensionless damping parameter, and $\boldsymbol{H}_{\text{eff}}$ is the effective field, consisting of the externally applied field, magnetostatic field, Heisenberg exchange field, and anisotropy field. In the simulation, we choose thickness $L_z = 3$ nm, width $L_y = 20$ nm, and length $L_x = 4096$ nm. Micromagnetic parameters are chosen to be the typical experimental values [22]: saturation magnetization $M_s = 9.1 \times 10^5$ A/m, exchange stiffness $A_{\text{ex}} = 1.4 \times 10^{-11}$ J/m, first-order uniaxial anisotropy constant $K_u = 8.4 \times 10^5$ J/m^3, and damping parameter $\alpha = 0.27$. The DW width is roughly given by $\Delta = \sqrt{A_{\text{ex}}/K_{\text{eff}}}$, where K_{eff} is the effective anisotropy, which includes the magnetocrystalline anisotropy K_u and the shape anisotropy. The discretization cell dimensions are $d_x = d_y = 2$ nm and $d_z = 0.5$ nm, smaller than the exchange length $L_{\text{ex}} = \sqrt{A_{\text{ex}}/(\mu_0 M_s^2)} \approx 3.7$ nm [24]. Periodic boundary conditions are used in the y direction to avoid boundary effects [25]. The LLG equation is then solved using the Dormand-Prince solver (RK45) with an adaptive time step.

The system is initialized in a configuration with two antiparallel out-of-plane (up and down) domains separated by a DW with an internal magnetization in the negative y direction, as shown in Fig. 1(a). The behavior of the DW in response to an external perpendicular magnetic field B_{ext} features unique, nonlinear dynamics that is understood very well [16]. Before the Walker breakdown, the average velocity increases linearly with external magnetic field, and after that, the velocity suddenly drops, signaling the onset of precession of the DW [26]. In the simulation, one can record the information about time-varying quantities $m_{x,y,z}(t)$, from which the DW dynamics can be further investigated. The average $\langle m_i \rangle$ $(i = x, y, z)$ is taken over a range extending 20 discretization cells around the DW. The instantaneous domain wall velocity is obtained as $v(t) \propto d\langle m_z \rangle/dt$ [27].

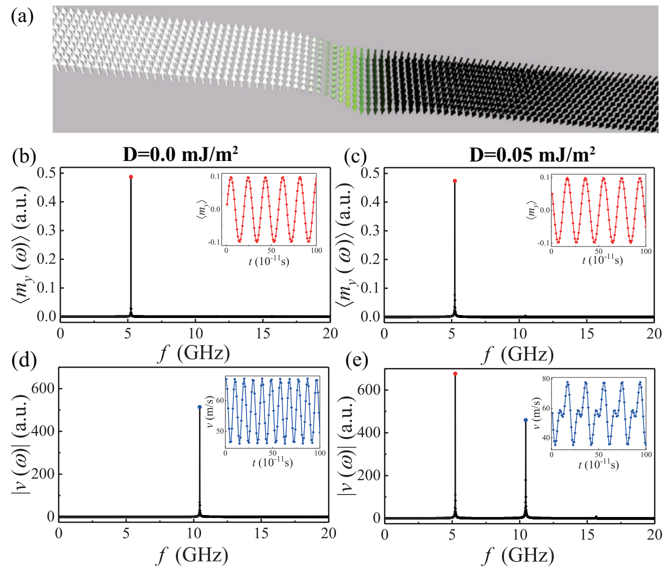

FIG. 1. (a) Schematic illustration of field-driven DW motion in a magnetic nanostrip. (b) and (c) Frequency spectra of $\langle m_y(t) \rangle$ without and with DMI, respectively. (d) and (e) Frequency spectra of $v(t)$ without and with DMI, respectively. The red and blue points correspond to the LFM and HFM peaks, respectively. Insets: $\langle m_y \rangle(t)$ (red dotted line) and $v_{\text{DW}}(t)$ (blue dotted line) signals. External field $B_{\text{ext}} = 200$ mT.

B. Method: Velocity frequency spectrum

In the precessional regime with zero DMI strength $D = 0$, we observe that both $\langle m_{x,y}(t) \rangle$ and $v(t)$ oscillate periodically with time, as shown in the insets of Figs. 1(b) and 1(d). However, they have different oscillating frequencies. The difference can be seen more clearly from the frequency spectrum of $\langle m_y(t) \rangle$ and $v(t)$. After a long time interval T, we carry out the fast Fourier transform of the instantaneous velocity $v(t)$:

$$v(\omega) = \frac{1}{\sqrt{T_m}} \int_0^{T_m} e^{i\omega t} v(t) dt. \tag{2}$$

A similar Fourier transform is also performed for $\langle m_y(t) \rangle$. In Figs. 1(b) and 1(d), we plot the magnitude of the Fourier transform $|\langle m_y(\omega) \rangle$ and $|v(\omega)|$ for the case of $D = 0$. It is clear that there is only a single peak in the frequency spectrum of $m_y(t)$ and $v(t)$. However, the peak frequency of the velocity is doubled that of m_y.

An interesting phenomenon appears when we introduce nonzero DMI. In the presence of DMI, the time-varying signal $\langle m_y(t) \rangle$ is almost the same as $D = 0$, and the oscillation frequency remains unchanged [inset of Fig. 1(c)]. However, the behavior of the velocity signal $v(t)$ changes radically, as shown in the inset of Fig. 1(e). Figures 1(c) and 1(e) plot the frequency spectra of $\langle m_y \rangle$ and $v(t)$ with nonzero DMI. While there is only one peak in the frequency spectrum of $\langle m_y \rangle$, two spectral peaks with different magnitudes emerge in $|v(\omega)|$. For convenience, we label the two oscillatory modes as

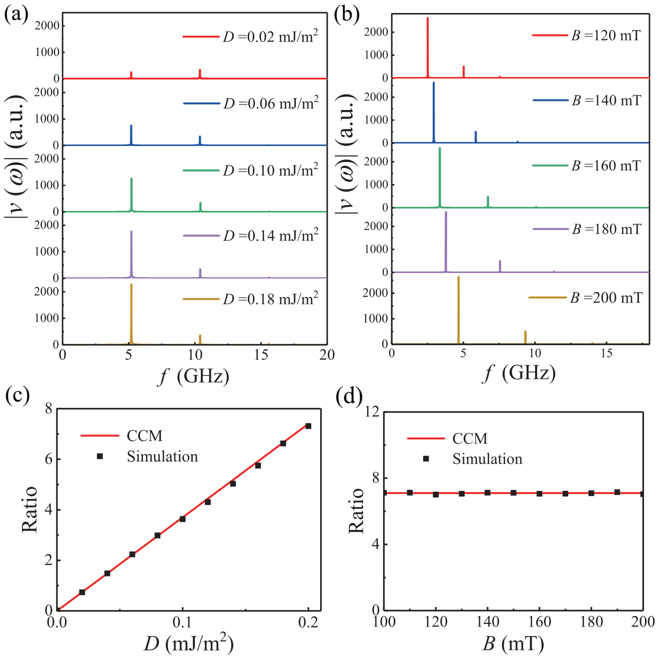

FIG. 2. Frequency spectrum of DW velocity $v(t)$ for different values of (a) D and (b) B_{ext}. Dependence of the ratio of LFM to HFM on (c) D and (d) B_{ext}. Squares are results from micromagnetic simulation, and the solid line shows results from the CCM.

the low-frequency mode (LFM) and the high-frequency mode (HFM).

We further investigate the influence of DMI strength D on the two emerging oscillating peaks in the velocity frequency spectrum. We first fix the external magnetic field B_{ext} and gradually increase the DMI strength D. As shown in Fig. 2(a), there are always two peaks in the velocity frequency spectrum with the frequencies remaining unchanged. However, with increasing DMI strength, the magnitude of the LFM peak increases, while the magnitude of the HFM peak remains unchanged. If we extract the LFM/HFM ratio from the frequency spectral data and plot it as a function of DMI intensity [Fig. 2(c)], we can see that the ratio increases linearly with the DMI strength D. We also study the velocity frequency spectrum under different external magnetic fields B_{ext} when the DMI strength is fixed, as shown in Figs. 2(b) and 2(d). Even though the oscillating frequency increases with increasing B_{ext}, the magnitude ratio of LFM/HMF remains unchanged as long as the DMI strength D is fixed.

This result confirms that the magnitude ratio of the two peaks in the velocity frequency spectrum is solely dependent on DMI and thus can be utilized as a measure of DMI strength. Later, we will show that this frequency spectrum analysis remains robust in the presence of external noise and pinning. In real experiments, one may encounter nanostrips with a wider width, for example, of the order of 1 μm. In this situation, some other dissipative effects would take place, such as pairs of vertical Bloch lines. Therefore, it would be interesting to discuss whether the appearance of Bloch lines would affect the accuracy of the approach. We leave the discussion to Appendix A.

III. COLLECTIVE-COORDINATE MODEL

To understand the underling physics of the above results obtained from the micromagnetic simulation, we resort to the collective-coordinate model, which can provide a semi-analytical solution to domain wall dynamics. Assuming that the DW remains a rigid object with constant width, the DW dynamics can be described by two independent variables, the DW position q and its conjugate momentum, the DW magnetization angle φ. The one-dimensional collective-coordinate model (CCM) reads [28–34]

$$v(t) \equiv \frac{dq}{dt} = \gamma' \Delta(\alpha H_a - H_K \sin 2\varphi + H_D \sin\varphi), \quad (3)$$

$$\frac{d\varphi}{dt} = \gamma'(H_a + \alpha H_K \sin 2\varphi - \alpha H_D \sin\varphi), \quad (4)$$

with $\gamma' = \frac{\gamma}{\alpha^2+1}$. Here, $H_K = 2K/(\mu_0 M_s)$, with K being the effective anisotropy energy, H_a is the external magnetic field applied along the easy axis, and $H_D = \pi D/(2\mu_0 M_s \Delta)$. Despite its simplicity, the CCM provides a quite accurate description of DW motion in a nanowire. It is also easy to generalize the equations to cases with external thermal noise or pinning disorder and to the system driven by electric current (see Sec. VI). Now we use Eqs. (3) and (4) to explain the emergence of two peaks in the velocity frequency spectrum in the presence of nonzero DMI.

Note that without external noise or disorder, the average magnetization $\langle m_y(t)\rangle$ is almost sinusoidal, as depicted in the insets of Figs. 1(b) and 1(c). Since $\langle m_y(t)\rangle$ is proportional to $\sin\varphi$, $\sin\varphi$ is also almost perfectly sinusoidal, with only a slight deviation. Actually, we can see this point simply from Eq. (4), which can be analytically solved if one of the two terms containing H_K and H_D vanishes. If $H_K = 0$, the solution of $\varphi(t)$ is given by

$$\tan\frac{\varphi}{2} = \frac{\sin(t'/2)}{\cos(t'/2+\theta)}, \quad (5)$$

with $t' = \gamma' H_a \sqrt{1-(\alpha H_D/H_a)^2}$ and $\theta = -\arcsin(\alpha H_D/H_a)$. The solution shows that if $\theta \ll 1$, i.e., $\alpha H_D \ll H_a$, then $\sin\varphi$ is very close to a sine function of time t, and the DW magnetization angle $\varphi(t)$ can be considered to increase almost linearly with time t. Indeed, direct calculations of the Fourier coefficients of $\sin\varphi$ show that a small deviation from linearity only results in the appearance of peaks at the nth harmonic frequency, but with a small amplitude that is of the order θ^{n-1} (see Appendix B for a detailed discussion). A similar discussion can be had for the case with nonzero H_K.

Under this consideration, we can qualitatively understand the previously observed phenomena from micromagnetic simulations. First, for the case of $H_D = 0$, the time-dependent part of the velocity in Eq. (3) is proportional to $\sin 2\varphi$, leading to a peak at the second harmonic frequency in the frequency spectrum. As we increase the DMI strength D, and thus H_D, an additional component proportional to $\sin\varphi$ appears and gives rise to a LFM in the velocity frequency spectrum. More importantly, in the limit that φ is almost linear in time t, the magnitude ratio of LFM to HFM is given from Eq. (3) by

$$\eta = \frac{H_D}{H_K} = \frac{\pi D}{4\Delta K}. \quad (6)$$

Therefore, we conclude that the magnitude of the DMI strength D can easily be obtained once we get the ratio η. The accuracy of this approach is guaranteed by $\alpha H_D/H_a \ll 1$ and $\alpha H_K/H_a \ll 1$, which can easily be achieved by increasing external field H_a.

IV. EXTERNAL NOISE AND PINNING DISORDER

We now proceed to verify the robustness of the frequency spectrum method and the accuracy of Eq. (6) in quantifying the DMI strength in the presence of external noise and pinning disorder. In this case, the time-varying velocity $v(t)$ is no longer a well-defined sinusoid. However, we can repeat the measurement many times during a short time interval and take the average of the fast Fourier transform $v(\omega)$. This method of data processing eliminates the effects of noise and disorder and provides the true information about the DMI strength.

We first investigate the effect of external noise on the velocity frequency spectrum. Without loss of generality, we consider the Gaussian white noise [35–38]. This type of noise commonly originates from experimental apparatuses [39], such as detectors [40], amplifiers [41], and ambient electromagnetic interference [35]. In the micromagnetic simulation, the effect of external noise can be introduced by the random field vector $\boldsymbol{h}_j$ on each site j, giving rise to an additional Zeeman energy $-M_s \sum_j \boldsymbol{h}_j \cdot \boldsymbol{m}_j$. Taking the average over all possible random field configurations, we have $\langle \boldsymbol{h}_j \rangle = 0$ and $\langle h_{i\alpha} h_{j\beta} \rangle = R^2 \delta_{i,j} \delta_{\alpha,\beta}$, where $\delta_{i,j}$ is the Kronecker delta function, $\alpha, \beta = x, y, z$, and R measures the disorder strength, i.e., the standard deviation of the employed random field distribution. In this paper, we adopt the Gaussian distribution [35] $\rho(h) = \exp(-h^2/2R^2)/(\sqrt{2\pi}R)$. Extensive simulations are conducted on system sizes up to $L_x = 2048$ for sufficiently strong noise $R = 10$ mT. The total time of simulation is 10^{-5} s, with 10^6 data points taken. To obtain the frequency spectrum, we divide the total time series into relatively short time intervals, with each time interval consisting of 10^4 data points. We then Fourier transform each short time interval and take the average of the Fourier transform $|v(\omega)|$ over all the time intervals. Figure 3(a) plots the velocity frequency spectrum, and the inset shows a snapshot of the time-varying velocity $v(t)$ with 200 data points. We can see that the velocity is strongly disturbed and is no longer a well-defined sinusoid. It is therefore hard to discern the information about DW dynamics simply from the profile of velocity. Nevertheless, after a sufficiently long time average, we can still obtain two peaks, identified as HFM and LFM in the velocity frequency spectrum, similar to the clean system. Here, the only difference is that, due to the external white noise, a nonzero background appears. Figure 3(c) plots the magnitude ratio of LFM to HFM as a function of DMI strength D when external noise is added. We find that for larger values of DMI, external noise has a more significant impact on $v_{\rm DW}$, resulting in larger errors in the ratio. We conclude that the method of the velocity frequency spectrum in determining the DMI strength is robust against external noise

We now consider the effect of intrinsic material defects in a real ferromagnetic nanostrip, which can significantly impact the behavior of domain walls [42–44]. These defects create potential wells in the micromagnetic energy landscape,

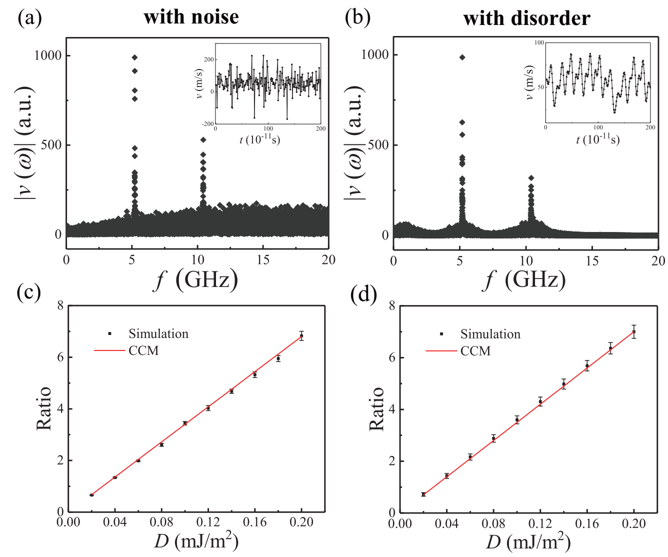

FIG. 3. Velocity frequency spectrum and magnitude ratio of LFM/HFM in the presence of external noise and pinning disorder. (a) and (b) The velocity frequency spectra with external noise and pinning disorder, respectively. Parameters are $D = 0.05\,\mathrm{mJ/m^2}$, $R = 10$ mT, and $r = 0.03$. The insets are the corresponding velocity signals. (c) and (d) The corresponding magnitude ratio vs DMI strength D. The error bars on the simulated data correspond to the uncertainties in the averaged magnitude of the frequency spectrum.

which can be characterized by the saturation magnetization and anisotropy between grains [45–47]. In this study, we investigate the properties of defects and propose a method to realistically incorporate their influence in two-dimensional numerical simulations. Our findings shed light on the complex behavior of domain walls in realistic nanostrips and highlight the need for a more comprehensive understanding of the impact of intrinsic material defects on their dynamics. For thin films with thicknesses of only a few atoms, a natural source of disorder is the thickness fluctuations of the film [48]. In order to account for the effect of quenched disorder, we construct "grains" with a linear size of 20 nm (defining the disorder correlation length) by Voronoi tessellation. Each grain has a normally distributed random thickness $t_G = h + \mathrm{Norm}(0, r)h$, with r being the relative magnitude of the grain-to-grain thickness variations and h being the mean thickness of the sample. $\mathrm{Norm}(0, r)$ denotes a normal distribution function with mean 0 and standard deviation r. These thickness fluctuations are then modeled using an approach proposed in Ref. [25] by modulating the saturation magnetization and anisotropy constant according to $M_s^G = M_s t_G/h$ and $K_u^G = K_u t_G/h$. Figures 3(b) and 3(d) present the velocity $v(t)$ over time, its frequency spectrum, and the ratio LFM/HFM as a function of DMI strength D in the presence of disorder. We can see that the profile of the velocity $v(t)$ is also perturbed, leading to a nonzero background and larger peak width in the frequency spectrum. However, the ratio η still linearly increases with DMI strength D, verifying the robustness of the frequency spectrum method.

The calculations with noise and disorder are also performed using the CCM. In the CCM, the effect of external noise can be introduced by the random field vector $\mathbf{h}$ on the external field H_a, and the effect of disorder can be included by introducing a pinning field $H_{\text{pin}}(x)$ which depends on the position x. The pinning field can be derived from an effective spatially dependent pinning potential $V_{\text{pin}}(x)$:

$$H_{\text{pin}}(x) = -\frac{1}{2\mu_0 M_s L_y L_z}\partial V_{\text{pin}}/\partial x. \tag{7}$$

The pinning potential can be chosen to be periodic with strength described by V_0:

$$V_{\text{pin}}(x) = V_0 \sin\left(\frac{\pi x}{p}\right), \tag{8}$$

where p is the spatial period.

V. SKEWNESS AND THIRD-ORDER CORRELATION

While the average, variance, and second-order correlation of physical quantities can provide much information about domain wall dynamics, more detailed information is actually concealed in the seemingly useless noisy data. Applying statistical methods to the noisy data, such as the distribution of the fluctuations, their moments, and the autocorrelation function, can yield a wealth of information about the underlying dynamics [49,50]. Here, we show that considering the third-order cumulant and third-order time-correlation function can reveal the intrinsic asymmetry induced by DMI. In full counting statistics, one can consider all orders of cumulants of a physical quantity, here, $\delta v(t) = v(t) - \langle v\rangle$:

$$c_n = \langle \delta v^n\rangle, \tag{9}$$

with the average taken over a long period of time. By definition, the first-order $c_1 = 0$. The second-order cumulant, i.e., the variance, describes the magnitude of fluctuation. The third-order cumulant c_3 is a measure of the asymmetry of the probability distribution of a real-valued random variable about its mean. To quantify the asymmetry, one can further define the skewness as

$$s = c_3/c_2^{3/2} \tag{10}$$

to renormalize the third-order cumulant by the variance. This skewness value can be positive, zero, negative, or undefined. In our case, as shown in Figs. 4(a) and 4(b), we can see that the skewness is always negative, and the magnitude of skewness increases in a roughly linear manner with D.

More detailed dynamical information can be revealed by studying the time-dependent correlation function [51,52]. Here, we consider the second-order and third-order correlation functions of velocity $v(t)$:

$$g_2(\tau) = \langle \delta v(0)\delta v(\tau)\rangle, \tag{11}$$

$$g_3(\tau_1, \tau_2) = \langle \delta v(0)\delta v(\tau_1)\delta v(\tau_1+\tau_2)\rangle/c_2^{3/2}. \tag{12}$$

The Fourier transformation of the second-order correlator $g_2(\tau)$ provides information similar to the frequency spectrum of $v(\omega)$. The third-order correlator g_3 normalized by the variance c_2 depends on two time variables and is expected to provide valuable information. In Figs. 4(c) and 4(d), $g_3(\tau_1, \tau_2)$ is plotted for the cases with $D = 0$ and $D \neq 0$, respectively. While g_3 is very small for the case with $D = 0$ (note the scale

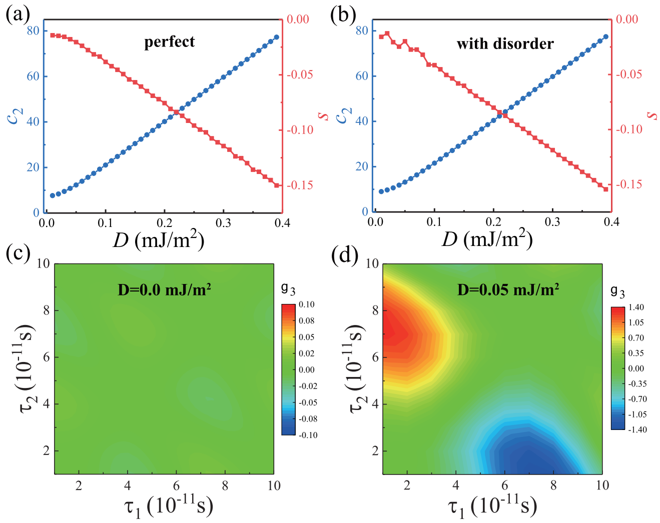

FIG. 4. Skewness and third-order correlator. The standard variance (blue) and skewness (red) in (a) the clean system and (b) a system with disorder. (c) and (d) The normalized third-order correlator $g_3(\tau_1, \tau_2)$ in the clean system for $D = 0$ mJ/m^2 and $D = 0.05$ mJ/m^2, respectively.

of the color bar), it becomes nonzero at finite time for the case with $D \neq 0$. More importantly, it displays a strong asymmetry with respect to τ_1 and τ_2, which should be a strong indication of the effect of DMI.

VI. DOMAIN WALL DYNAMICS DRIVEN BY ELECTRIC CURRENT

In ferromagnetic nanowires, the DW can also be driven by spin-polarized electrical currents due to the spin transfer torque (STT) exerted on the local magnetization. Including the STT, the LLG equation can be written as [31]

$$\frac{\partial \boldsymbol{m}}{\partial t} = -\gamma \boldsymbol{m}\times \boldsymbol{H}_{\text{eff}} + \alpha \boldsymbol{m}\times\frac{\partial \boldsymbol{m}}{\partial t} + b_J(\hat{\boldsymbol{j}}\cdot\nabla)\boldsymbol{m} - c_J\boldsymbol{m}\times(\hat{\boldsymbol{j}}\cdot\nabla)\boldsymbol{m}. \tag{13}$$

The first and second terms have been introduced in Sec. II A the main text. The third term is the adiabatic STT $b_J = P\mu_B j/eM_s$, with e being the electron charge, P being the spin polarization, μ_B being the Bohr magneton, j being the magnitude of the current, and M_s being the saturation magnetization. Here, $\hat{\boldsymbol{j}}$ is the unit vector of the local current density. The fourth term is the nonadiabatic STT, with c_J being the magnitude of nonadiabticity. Usually, one introduces a dimensionless parameter $\xi = c_J/b_J$ to represent the nonadiabaticity.

In Fig. 5, we plot the frequency spectrum of $\langle m_y(t)\rangle$ and $v(t)$ for the cases with and without DMI. In the precessional regime with zero DMI strength $D = 0$, we observe that both $\langle m_{x,y}(t)\rangle$ and $v(t)$ oscillate periodically with time, as shown in the insets of Fig. 5. However, they have different oscillating frequencies. In Figs. 5(a) and 5(c), we plot the magnitude of the Fourier transform $|\langle m_y(\omega)\rangle$ and $|v(\omega)|$ for the case with $D = 0$. It is shown that there is only one single peak in the frequency spectrum of $m_y(t)$ and $v(t)$. However, the peak frequency of the velocity is double that of m_y.

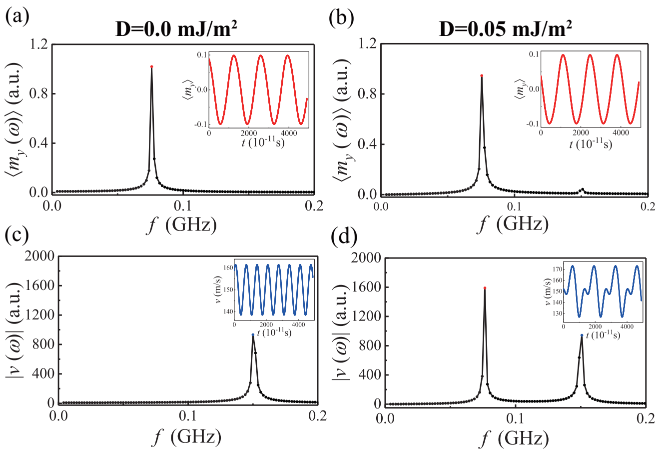

FIG. 5. Frequency spectra of $\langle m_y(t)\rangle$ (a) without and (b) with DMI. Frequency spectra of $v(t)$ (c) without and (c) with DMI. The red and blue points correspond to the LFM and HFM peaks, respectively. Insets: $\langle m_y\rangle(t)$ (red dotted line) and $v(t)$ (blue dotted line) signals. Electric current $j = 3 \times 10^{12}\mathrm{A/m^2}$, spin polarization $P = 0.8$, and nonadiabaticity $\xi = 0.04$.

In the presence of DMI, the time-varying signal $\langle m_y(t)\rangle$ is almost the same as $D = 0$, and the oscillation frequency remains unchanged [inset of Fig. 5(b)]. However, the behavior of the velocity signal $v(t)$ changes radically, as shown in the inset of Fig. 5(d). Figures 5(b) and 5(d) plot the frequency spectra of $\langle m_y\rangle$ and $v(t)$ with nonzero DMI. Two spectral peaks with different magnitudes in $|v(\omega)|$ emerge.

We further investigate the influence of DMI strength D on the two emerging oscillating peaks in the velocity frequency spectrum. We first fix the magnitude of the electric current J and gradually increase the DMI strength D. As shown in Fig. 6(a), there are always two peaks in the velocity frequency spectrum with the frequencies remaining unchanged. However, with increasing DMI strength, the magnitude of the LFM peak increases, while the magnitude of the HFM peak remains unchanged. If we extract the LFM/HFM ratio from the frequency spectral data and plot it as a function of DMI intensity [Fig. 6(c)], we can see that the ratio linearly increases with the DMI strength D. We also study the velocity frequency spectrum under different electric currents J when the DMI strength is fixed, as shown in Figs. 6(b) and 6(d). Even though the oscillating frequency increases with increasing J, the magnitude ratio of LFM/HMF remains unchanged as long as the DMI strength D is fixed.

In the current-driven case, we can also introduce the collective-coordinate model as follows:

$$\frac{d\varphi}{dt} + \alpha\frac{1}{\Delta}\frac{dq}{dt} = \frac{c_J}{\Delta}, \tag{14}$$

$$\alpha\frac{d\varphi}{dt} - \frac{1}{\Delta}\frac{dq}{dt} = \frac{b_J}{\Delta} + \gamma H_K \sin 2\varphi - \gamma H_D \sin\varphi. \tag{15}$$

Compared with the magnetic field driven case, the difference is the substitution of γH_a by c_J/Δ and an additional term of b_J/Δ. Figure 6 shows that the results of the CCM agree well with those of micromagnetic simulation.

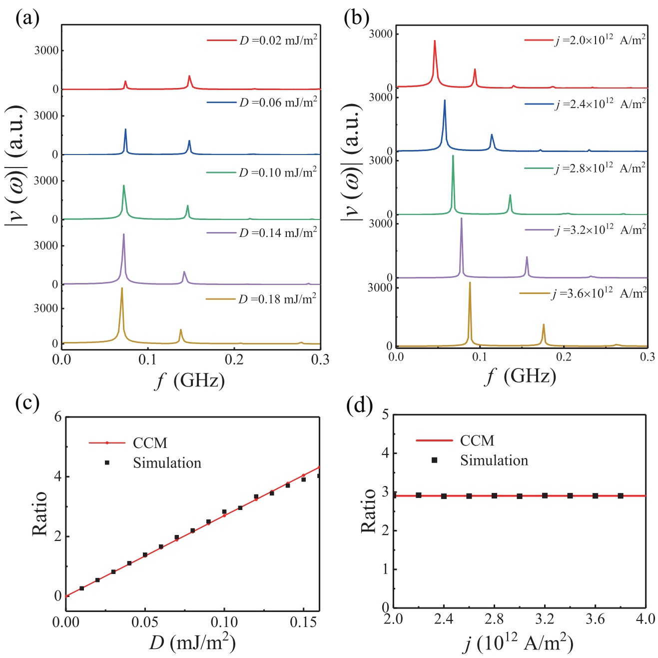

FIG. 6. Frequency spectrum of DW velocity $v(t)$ for different values of (a) D and (b) current j. Dependence of the ratio of LFM to HFm on (c) D and (d) J. Squares are results from the micromagnetic simulation, and the solid line shows results from the CCM. Parameters are $P = 0.8$, $\xi = 0.04$, and $j = 3 \times 10^{12}\mathrm{A/m^2}$ in (a) and $D = 0.1\mathrm{mJ/m^2}$ in (b).

VII. DISCUSSION AND CONCLUSION

We demonstrated that statistical analysis of the domain wall dynamics can be a powerful tool for quantifying DMI strength and can provide more detailed information about the effects induced by DMI. Since our approach takes a long time average of the domain wall dynamics, the velocity frequency spectrum method is robust against external noise and pinning disorder. Moreover, the third-order cumulant and third-order time-dependent correlation function of the velocity were calculated and shown to yield valuable information regarding the asymmetry induced by DMI. Our findings offer a comprehensive understanding of the dynamics of domain walls in the presence of DMI and provide important insights for the development of novel DW-based devices.

For the experimental application of our approach, one could resort to the optical spin noise spectroscopy technique, which utilizes the rotation of a linearly polarized laser light beam by Faraday rotation or the Kerr effect and has matured into an effective and versatile technique to extract the full spin dynamics even at thermal equilibrium. Recently, it was shown that combining ultrafast laser spectroscopy with the spin noise spectroscopy technique enables one to extend the detectable frequencies up to 16 GHz of spin dynamics [53]. It was also reported that high-sensitivity spin noise spectroscopy has the resolution of a single central spin in a quantum dot and is capable of measuring the extremely long spin coherence of single-spin dynamics enclosed in individual quantum dots [54]. Therefore, we expect that in the near future, it will be possible to apply spin noise spectroscopy with high time resolution and spatial resolution to the study of domain

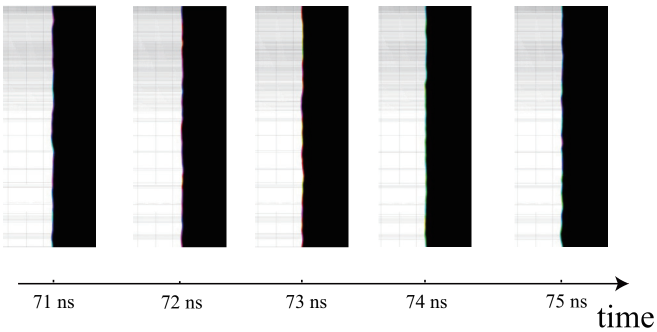

FIG. 7. Snapshots of the wider strips' domain wall (with disorder).

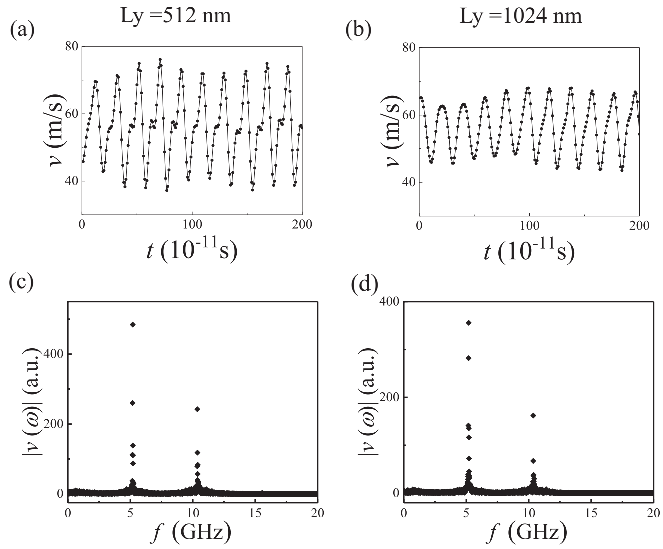

FIG. 8. Wider strips' velocity signals and velocity frequency spectrum in the presence of disorder with different strip widths L_y. Parameters are $D = 0.05$ mJ/m^2 and $B = 200$ mT.

wall dynamics. Moreover, there may be other new experimental techniques that could be applied to the study of domain dynamics. For example, the nitrogen vacancy center based superresolution quantum magnetometer can achieve a spatial resolution of 30 nm [55] and a time resolution of 20 ns [56].

ACKNOWLEDGMENTS

This work was supported by the National Key Research and Development Program of the Ministry of Science and Technology (Grant No. 2021YFA1200700), the National Natural Science Foundation of China (Grants No. 11905054, No. 12275075, and No. 12105094), and the Fundamental Research Funds for the Central Universities from China.

APPENDIX A: DOMAIN WALL DYNAMICS OF A WIDE NANOSTRIP WITH BLOCH LINES

In the main text, we discussed the robustness of our approach against disorder and pinning for a nanostrip with a width up to 20 nm. In real experiments, one may encounter a nanostrip with a larger width, for example, of the order of 1 μm. In this situation, some other dissipative effects would take place, such as pairs of vertical Bloch lines [57]. Therefore, it would be interesting to discuss whether the appearance of Bloch lines would affect the accuracy of our approach. For this purpose, we performed a micromagnetic simulation on a nanostrip with a width up to $L_y = 1024$ nm. Figure 7 shows that in the presence of disorder, vertical Bloch lines appear, which will affect the domain wall dynamics. We then record the velocity signals and calculate the velocity frequency spectrum for different strip widths L_y. In Fig. 8, we can see that the width of the strip indeed affects the velocity profile, which is no longer a very well defined sinusoid. However, after a long time average, in the velocity frequency spectrum, there are still two peaks, and more importantly, the ratio of the two peaks agrees well with the case with narrow width. This means that our approach is also robust against the appearance of Bloch lines. The underlying reason may be that our approach is basically an averaging result of a long time dynamics during which the pinning effect or the effect of Bloch point does not play an important role in the total process.

APPENDIX B: EXACT SOLUTION OF φ IN THE COLLECTIVE-COORDINATE MODEL AND ITS FOURIER COEFFICIENTS

From the equations of motion in the collective-coordinate model

$$\frac{d\varphi}{dt} + \alpha\frac{1}{\Delta}\frac{dq}{dt} = \gamma H_a, \tag{B1}$$

$$\frac{1}{\gamma}\left(\alpha\frac{d\varphi}{dt} - \frac{1}{\Delta}\frac{dq}{dt}\right) = H_K \sin 2\varphi - H_D \sin\varphi, \tag{B2}$$

we can obtain the equation for φ:

$$\frac{d\varphi}{dt} = \frac{\gamma}{1+\alpha^2}(H_a + \alpha H_K \sin 2\varphi - \alpha H_D \sin\phi). \tag{B3}$$

We will show that if $\alpha H_K \ll H_a$ and $\alpha H_D \ll H_a$, our approach has high precision in quantifying the DMI strength. This equation is analytically solvable if $H_K = 0$ or $H_D = 0$. We first consider the case with $H_K = 0$ and study the following reduced equation:

$$\varphi_t = 1 + a\sin\varphi, \tag{B4}$$

which can be obtained by making the time rescale $t \to (1+\alpha^2)t/(\gamma H_a)$ and setting $a = -\alpha H_D/H_a$. Equation (B4) can be solved analytically. Its solution is given by

$$\tan\frac{\varphi}{2} = \frac{\sin(t'/2)}{\cos(t'/2+\theta)}, \tag{B5}$$

with $\theta = \arcsin a$ and $t' = \sqrt{1-a^2}t$. Therefore,

$$\sin\varphi = \frac{\sin(t'+\theta) - \sin\theta}{1 - \sin(t'+\theta)\sin\theta} \tag{B6}$$

and

$$\sin(2\varphi) = \frac{4\cos\theta\cos(t'+\theta)[\sin(t'+\theta) - \sin\theta]}{[1-\sin(t'+\theta)\sin\theta]^2}. \tag{B7}$$

We can see that $\sin\varphi$ is a periodic function of rescaled time t' with period 2π. Now we can calculate the Fourier series of $\sin\varphi$ and $\sin 2\varphi$. For $\sin\varphi$, the Fourier coefficients are given by

$$A_n^{(1)} = \int \frac{dt'}{2\pi}\sin[\varphi(t')]e^{\mathrm{int}'}, \tag{B8}$$

with $n = 1, 2, 3, \ldots$. This integral can be performed in the complex plane by introducing $z = e^{it'}$, and the integration contour is along the unit circle. Using the residual theorem, this integration can be performed exactly:

$$A_1^{(1)} = i\frac{\cos\theta}{1+\cos\theta}, \tag{B9}$$

$$A_2^{(1)} = -4\cos\theta\frac{\sin^4(\theta/2)}{\sin^3\theta}. \tag{B10}$$

In the limit of small $a \ll 1$, and thus $\theta \ll 1$, we can see that $|A_1^{(1)}| \sim 1/2$, while $|A_2^{(1)}| \sim a/4$, which is much smaller than $|A_1^{(1)}|$. Similarly, the magnitude of higher-order harmonics $|A_n^{(1)}|$ with $n > 1$ is of the order of a^{n-1}.

For $\sin[2\varphi(t)]$, its Fourier series are quite different. The coefficients can be obtained similarly:

$$A_1^{(2)} = -\sin\frac{\theta}{2}\frac{\cos\theta}{\cos^3(\theta/2)}, \tag{B11}$$

$$A_2^{(2)} = \frac{i}{2}\cos\theta(2\cos\theta-1)\sec^4(\theta/2). \tag{B12}$$

For small θ, $|A_1^{(2)}| \sim \theta/2$, and $|A_2^{(2)}| \sim 1/2$. This means that $\sin[2\varphi(t)]$ has the largest Fourier component at the second harmonic frequency.

For the case with $H_D = 0$ but $H_K \neq 0$, we encounter a differential equation as follows:

$$\varphi_t = 1 + a\sin(2\varphi), \tag{B13}$$

which can be solved as before by making variable changes: $\varphi \to \varphi/2$ and $t \to t/2$. The solution is given by

$$\tan\varphi = \frac{\sin(t')}{\cos(t'+\theta)}, \tag{B14}$$

with $\theta = \arcsin a$ and $t' = \sqrt{1-a^2}t$. Further,

$$\sin\varphi = \frac{\sin t'}{\sqrt{1-\sin(2t'+\theta)\sin\theta}}, \tag{B15}$$

$$\sin(2\varphi) = \frac{\sin(2t'+\theta)-\sin\theta}{1-\sin(2t'+\theta)\sin\theta}. \tag{B16}$$

In this case, the largest Fourier coefficient of $\sin\varphi$ is at the basic harmonic frequency, and its amplitude is approximately $1/2$ if θ is small. The magnitude of higher-order harmonics is of the order of $o(\theta^n)$. For $\sin(2\varphi)$, the Fourier coefficients can be obtained analytically, and the largest coefficient is at the second harmonic frequency, with amplitude given by $\frac{\cos\theta}{1+\cos\theta}$, which reduces to $1/2$ in the limit of $\theta \to 0$.

The above analysis shows that in the presence of either H_K or H_D, the largest Fourier component of $\sin\varphi$ is always at the basic harmonic frequency, while the largest Fourier component of $\sin(2\varphi)$ is at the second harmonic frequency. Therefore, according to the equation of motion of the velocity $v(t)$, the ratio of LFM to HFM in the frequency spectrum is a good estimation of the ratio of coefficients of the $\sin\varphi$ term to the $\sin(2\varphi)$ term, as long as $\alpha H_K \ll H_a$ and $\alpha H_D \ll H_a$. This condition can be easily satisfied by increasing the external magnetic field by H_a.

We can also use perturbation theory to study the case with both H_K and H_d being nonzero. Now we encounter the following equation:

$$\varphi_t = 1 + a_1\sin\varphi + a_2\sin(2\varphi), \tag{B17}$$

with $a_1 \ll 1$ and $a_2 \ll 1$. Integrating this equation, we have

$$\begin{aligned} t &= \int d\varphi\frac{1}{1+a_1\sin\varphi+a_2\sin(2\varphi)} \\ &\sim \int d\varphi[1-a_1\sin\varphi-a_2\sin(2\varphi)] \\ &= \varphi + a_1\cos\varphi + a_2\cos(2\varphi). \end{aligned} \tag{B18}$$

To zeroth-order perturbation of a_1 and a_2, we have simply $\varphi = t$. To first-order perturbation, we have

$$\varphi = t - a_1\cos t - a_2\cos(2t). \tag{B19}$$

Inserting this back into the equation for the velocity, we have, up to first order of a_1 and a_2,

$$v(t) \sim \gamma' H_a[1 + a_1\sin t + a_2\sin(2t)]. \tag{B20}$$

Its Fourier coefficients at basic and second harmonic frequencies are $\gamma' H_a a_1$ and $\gamma' H_a a_2$, respectively. The ratio of the two is simply H_D/H_K.

[1] L. Wang, N. Chepiga, D.-K. Ki, L. Li, F. Li, W. Zhu, Y. Kato, O. S. Ovchinnikova, F. Mila, I. Martin, D. Mandrus, and A. F. Morpurgo, Controlling the topological sector of magnetic solitons in exfoliated $Cr_{1/3}NbS_2$ Crystals, Phys. Rev. Lett. **118**, 257203 (2017).

[2] K. von Bergmann, A. Kubetzka, O. Pietzsch, and R. Wiesendanger, Interface-induced chiral domain walls, spin spirals and skyrmions revealed by spin-polarized scanning tunneling microscopy, J. Phys.: Condens. Matter **26**, 394002 (2014).

[3] X. Li, C. Collignon, L. Xu, H. Zuo, A. Cavanna, U. Gennser, D. Mailly, B. Fauque, L. Balents, Z. Zhu, and K. Behnia, Chiral domain walls of Mn_3Sn and their memory, Nat. Commun. **10**, 3021 (2019).

[4] A. Brataas, Chiral domain walls move faster, Nat. Nanotechnol. **8**, 485 (2013).

[5] A. Fert, N. Reyren, and V. Cros, Magnetic skyrmions: Advances in physics and potential applications, Nat. Rev. Mater. **2**, 17031 (2017).

[6] G. Finocchio, F. Büttner, R. Tomasello, M. Carpentieri, and M. Kläui, Magnetic skyrmions: Advances in physics and potential applications, J. Phys. D **49**, 423001 (2016).

[7] X. Zhang, Y. Zhou, K. M. Song, T.-E. Park, J. Xia, M. Ezawa, X. Liu, W. Zhao, G. Zhao, and S. Woo, Skyrmion-electronics:

Writing, deleting, reading and processing magnetic skyrmions toward spintronic applications, J. Phys.: Condens. Matter **32**, 143001 (2020).

[8] S. Wolf, D. Awschalom, R. Buhrman, J. Daughton, S. von Molnár, M. Roukes, A. Y. Chtchelkanova, and D. Treger, Spintronics: A spin-based electronics vision for the future, Science **294**, 1488 (2001).

[9] S. Li, H. Nakamura, T. Kanazawa, X. Liu, and A. Morisako, Current-induced domain wall motion in TbFeCo wires with perpendicular magnetic anisotropy, IEEE Trans. Magn. **46**, 1695 (2010).

[10] P. Shepley, A. Rushforth, M. Wang, G. Burnell, and T. Moore, Modification of perpendicular magnetic anisotropy and domain wall velocity in Pt/Co/Pt by voltage-induced strain, Sci. Rep. **5**, 7921 (2015).

[11] T. Koyama, G. Yamada, H. Tanigawa, S. Kasai, N. Ohshima, S. Fukami, N. Ishiwata, Y. Nakatani, and T. Ono, Control of domain wall position by electrical current in structured Co/Ni wire with perpendicular magnetic anisotropy, Appl. Phys. Express **1**, 101303 (2008).

[12] T. Ha Pham, J. Vogel, J. Sampaio, M. Vaňatka, J.-C. Rojas-Sánchez, M. Bonfim, D. Chaves, F. Choueikani, P. Ohresser, E. Otero *et al.*, Very large domain wall velocities in Pt/Co/GdOx and Pt/Co/Gd trilayers with Dzyaloshinskii-Moriya interaction, Europhys. Lett. **113**, 67001 (2016).

[13] M. Carpentieri, R. Tomasello, R. Zivieri, and G. Finocchio, Topological, non-topological and instanton droplets driven by spin-transfer torque in materials with perpendicular magnetic anisotropy and Dzyaloshinskii–Moriya Interaction, Sci. Rep. **5**, 16184 (2015).

[14] W. Lin, B. Yang, A. P. Chen, X. Wu, R. Guo, S. Chen, L. Liu, Q. Xie, X. Shu, Y. Hui, G. M. Chow, Y. Feng, G. Carlotti, S. Tacchi, H. Yang, and J. Chen, Perpendicular magnetic anisotropy and Dzyaloshinskii-Moriya interaction at an oxide/ferromagnetic metal interface, Phys. Rev. Lett. **124**, 217202 (2020).

[15] A. Mougin, M. Cormier, J. Adam, P. Metaxas, and J. Ferré, Domain wall mobility, stability and Walker breakdown in magnetic nanowires, Europhys. Lett. **78**, 57007 (2007).

[16] A. Thiaville, S. Rohart, É. Jué, V. Cros, and A. Fert, Dynamics of Dzyaloshinskii domain walls in ultrathin magnetic films, Europhys. Lett. **100**, 57002 (2012).

[17] M. Kuepferling, A. Casiraghi, G. Soares, G. Durin, F. Garcia-Sanchez, L. Chen, C. H. Back, C. H. Marrows, S. Tacchi, and G. Carlotti, Measuring interfacial Dzyaloshinskii-Moriya interaction in ultra thin films, Rev. Mod. Phys. **95**, 015003 (2023).

[18] K. Zakeri, Y. Zhang, J. Prokop, T.-H. Chuang, N. Sakr, W.-X. Tang, and J. Kirschner, Asymmetric spin-wave dispersion on Fe (110): Direct evidence of the Dzyaloshinskii-Moriya interaction, Phys. Rev. Lett. **104**, 137203 (2010).

[19] J.-H. Moon, S.-M. Seo, K.-J. Lee, K.-W. Kim, J. Ryu, H.-W. Lee, R. D. McMichael, and M. D. Stiles, Spin-wave propagation in the presence of interfacial Dzyaloshinskii-Moriya interaction, Phys. Rev. B **88**, 184404 (2013).

[20] J. P. Garcia, A. Fassatoui, M. Bonfim, J. Vogel, A. Thiaville, and S. Pizzini, Magnetic domain wall dynamics in the precessional regime: Influence of the Dzyaloshinskii-Moriya interaction, Phys. Rev. B **104**, 014405 (2021).

[21] R. Soucaille, M. Belmeguenai, J. Torrejon, J.-V. Kim, T. Devolder, Y. Roussigné, S.-M. Chérif, A. Stashkevich, M. Hayashi, and J.-P. Adam, Probing the Dzyaloshinskii-Moriya interaction in CoFeB ultrathin films using domain wall creep and Brillouin light spectroscopy, Phys. Rev. B **94**, 104431 (2016).

[22] P. Metaxas, J. Jamet, A. Mougin, M. Cormier, J. Ferré, V. Baltz, B. Rodmacq, B. Dieny, and R. Stamps, Creep and flow regimes of magnetic domain-wall motion in ultrathin Pt/Co/Pt films with perpendicular anisotropy, Phys. Rev. Lett. **99**, 217208 (2007).

[23] A. Vansteenkiste, J. Leliaert, M. Dvornik, M. Helsen, F. Garcia-Sanchez, and B. Van Waeyenberge, The design and verification of MuMax3, AIP Adv. **4**, 107133 (2014).

[24] G. S. Abo, Y.-K. Hong, J. Park, J. Lee, W. Lee, and B.-C. Choi, Definition of magnetic exchange length, IEEE Trans. Magn. **49**, 4937 (2013).

[25] T. Herranen and L. Laurson, Barkhausen noise from precessional domain wall motion, Phys. Rev. Lett. **122**, 117205 (2019).

[26] N. L. Schryer and L. R. Walker, The motion of 180 domain walls in uniform dc magnetic fields, J. Appl. Phys. **45**, 5406 (1974).

[27] J. Vandermeulen, B. Van de Wiele, A. Vansteenkiste, B. Van Waeyenberge, and L. Dupré, A collective coordinate approach to describe magnetic domain wall dynamics applied to nanowires with high perpendicular anisotropy, J. Phys. D **48**, 035001 (2015).

[28] O. A. Tretiakov and A. Abanov, Current driven magnetization dynamics in ferromagnetic nanowires with a Dzyaloshinskii-Moriya interaction, Phys. Rev. Lett. **105**, 157201 (2010).

[29] Z. Sun, P. Fang, X. Shi, X. Wang, and F. Li, Field-driven side-by-side magnetic domain wall dynamics in ferromagnetic nanostrips, Phys. Rev. B **106**, 014412 (2022).

[30] S.-W. Jung, W. Kim, T.-D. Lee, K.-J. Lee, and H.-W. Lee, Current-induced domain wall motion in a nanowire with perpendicular magnetic anisotropy, Appl. Phys. Lett. **92**, 202508 (2008).

[31] O. Boulle, S. Rohart, L. Buda-Prejbeanu, E. Jué, I. Miron, S. Pizzini, J. Vogel, G. Gaudin, and A. Thiaville, Domain wall tilting in the presence of the Dzyaloshinskii-Moriya interaction in out-of-plane magnetized magnetic nanotracks, Phys. Rev. Lett. **111**, 217203 (2013).

[32] E. Martinez, S. Emori, N. Perez, L. Torres, and G. S. Beach, Current-driven dynamics of Dzyaloshinskii domain walls in the presence of in-plane fields: Full micromagnetic and one-dimensional analysis, J. Appl. Phys. **115**, 213909 (2014).

[33] R. Lo Conte, E. Martinez, A. Hrabec, A. Lamperti, T. Schulz, L. Nasi, L. Lazzarini, R. Mantovan, F. Maccherozzi, S. S. Dhesi, B. Ocker, C. H. Marrows, T. A. Moore, and M. Klaui, Role of B diffusion in the interfacial Dzyaloshinskii-Moriya interaction in Ta/$Co_{20}Fe_{60}B_{20}$/MgO nanowires, Phys. Rev. B **91**, 014433 (2015).

[34] M. Lucassen, H. Van Driel, C. M. Smith, and R. Duine, Current-driven and field-driven domain walls at nonzero temperature, Phys. Rev. B **79**, 224411 (2009).

[35] D. Jovković, S. Janićević, S. Mijatović, L. Laurson, and D. Spasojević, Effects of external noise on threshold-induced correlations in ferromagnetic systems, Phys. Rev. E **103**, 062114 (2021).

[36] D. Spasojević, S. Graovac, and S. Janićević, Interplay of disorder and type of driving in disordered ferromagnetic systems, Phys. Rev. E **106**, 044107 (2022).

[37] E. Gopalakrishnan and R. Sujith, Effect of external noise on the hysteresis characteristics of a thermoacoustic system, J. Fluid Mech. **776**, 334 (2015).

[38] S. Janićević, D. Knežević, S. Mijatović, and D. Spasojević, Scaling domains in the nonequilibrium athermal random field Ising model of finite systems, J. Stat. Mech. **2021**, 013202.

[39] H. Bittel, Noise of ferromagnetic materials, IEEE Trans. Magn. **5**, 359 (1969).

[40] T. Kaisar, M. M. Rajib, H. ElBidweihy, M. Barbic, and J. Atulasimha, Modeling of magnetization dynamics and thermal magnetic moment fluctuations in nanoparticle-enhanced magnetic resonance detection, J. Appl. Phys. **129**, 214505 (2021).

[41] Y. Netzer, The design of low-noise amplifiers, Proc. IEEE **69**, 728 (1981).

[42] H. Tanigawa, T. Koyama, M. Bartkowiak, S. Kasai, K. Kobayashi, T. Ono, and Y. Nakatani, Dynamical pinning of a domain wall in a magnetic nanowire induced by walker breakdown, Phys. Rev. Lett. **101**, 207203 (2008).

[43] N. B. Caballero, E. E. Ferrero, A. B. Kolton, J. Curiale, V. Jeudy, and S. Bustingorry, Magnetic domain wall creep and depinning: A scalar field model approach, Phys. Rev. E **97**, 062122 (2018).

[44] V. Jeudy, R. D. Pardo, W. S. Torres, S. Bustingorry, and A. B. Kolton, Pinning of domain walls in thin ferromagnetic films, Phys. Rev. B **98**, 054406 (2018).

[45] P. Gaunt, Ferromagnetic domain wall pinning by a random array of inhomogeneities, Philos. Mag. B **48**, 261 (1983).

[46] M. Kläui, H. Ehrke, U. Rüdiger, T. Kasama, R. E. Dunin-Borkowski, D. Backes, L. J. Heyderman, C. A. Vaz, J. A. C. Bland, G. Faini *et al.*, Direct observation of domain-wall pinning at nanoscale constrictions, Appl. Phys. Lett. **87**, 102509 (2005).

[47] S. Moretti, M. Voto, and E. Martinez, Dynamical depinning of chiral domain walls, Phys. Rev. B **96**, 054433 (2017).

[48] S. Zapperi, P. Cizeau, G. Durin, and H. E. Stanley, Dynamics of a ferromagnetic domain wall: Avalanches, depinning transition, and the Barkhausen effect, Phys. Rev. B **58**, 6353 (1998).

[49] H. Qian and E. L. Elson, Fluorescence correlation spectroscopy with high-order and dual-color correlation to probe nonequilibrium steady states, Proc. Natl. Acad. Sci. USA **101**, 2828 (2004).

[50] Y. Chen, X. Ge, W. Luo, S. Liang, X. Yang, L. You, Y. Zhang, and Z. Yuan, Chaotic precession of antiferromagnetic domain walls, Phys. Rev. B **107**, L020405 (2023).

[51] B. M. McCoy, J. H. Perk, and R. E. Shrock, Time-dependent correlation functions of the transverse Ising chain at the critical magnetic field, Nucl. Phys. B **220**, 35 (1983).

[52] G. Schütz, Time-dependent correlation functions in a one-dimensional asymmetric exclusion process, Phys. Rev. E **47**, 4265 (1993).

[53] G. M. Müller, M. Römer, J. Hübner, and M. Oestreich, Gigahertz spin noise spectroscopy in *n*-doped bulk GaAs, Phys. Rev. B **81**, 121202(R) (2010).

[54] D. Farfurnik, H. Singh, Z. Luo, A. S. Bracker, S. G. Carter, R. M. Pettit, and E. Waks, All-optical noise spectroscopy of a solid-state spin, Nano Lett. **23**, 1781 (2023).

[55] J. Zopes and C. L. Degen, Reconstruction-free quantum sensing of arbitrary waveforms, Phys. Rev. Appl. **12**, 054028 (2019).

[56] K. Chang, A. Eichler, J. Rhensius, L. Lorenzelli, and C. L. Degen, Nanoscale imaging of current density with a single-spin magnetometer, Nano Lett. **17**, 2367 (2017).

[57] M. Voto, L. Lopez-Diaz, and L. Torres, Effects of grain size and disorder on domain wall propagation in CoFeB thin films, J. Phys. D **49**, 185001 (2016).